Eur. J. Mineral., 36, 845–862, 2024
https://doi.org/10.5194/ejm-36-845-2024

European Journal of Mineralogy
Open Access

Chrome incorporation in high-pressure Fe–Mg oxides

Alan B. Woodland[1], Katrin Schumann[1], Laura Uenver-Thiele[1], Kevin Rosbach[1], Tiziana Boffa Ballaran[2], Caterina Melai[2,a], and Elena Bykova[1]

[1]Institut für Geowissenschaften, Universität Frankfurt, 60438 Frankfurt am Main, Germany
[2]Bayerisches Geoinstitut, Universität Bayreuth, 95440 Bayreuth, Germany
[a]now at: Department of Geology, Trinity College Dublin, College Green, Dublin 2, Ireland

Correspondence: Alan B. Woodland (woodland@em.uni-frankfurt.de)

Received: 19 April 2024 – Revised: 16 July 2024 – Accepted: 22 July 2024 – Published: 19 September 2024

Abstract. The occurrence of Cr-bearing oxide phases as inclusions in diamonds and in extraterrestrial materials has the potential to serve as an indicator of formation conditions. However, such an application requires detailed knowledge of phase stabilities and the influence that Cr may have on its stability. To this end, the incorporation of Cr in high-pressure post-spinel Fe–Mg oxide phases was experimentally investigated at pressures of 14–22 GPa and temperatures between 1100 and 1600 °C using a multi-anvil press. We find that neither the $Fe_3Cr_2O_6$ nor the $Mg_3Cr_2O_6$ endmember composition is stable over the expected range of pressure and temperature where Fe_5O_6 itself is known to be stable. Further experiments along the $Fe_3^{2+}Fe_2^{3+}O_6$–$Fe_3^{2+}Cr_2O_6$ binary indicate only small amounts of Cr substitution are possible: ∼ 0.12 cations Cr per formula unit or ∼ 6 mol % $Fe_3^{2+}Cr_2O_6$ component. In contrast, complete solid solution is apparent across both the $Fe_2^{2+}(Cr,Fe^{3+})_2O_5$ and the $Mg_2(Cr,Fe^{3+})_2O_5$ binaries, and there are indications of complete solution in the entire $(Mg,Fe^{2+})_2(Cr,Fe^{3+})_2O_5$ quaternary system. The O_5-structured phase usually coexists with (Fe,Mg)O. At 16–20 GPa, a post-spinel phase with O_4 stoichiometry was occasionally encountered, having either a modified Ca-ferrite- (mCF-$FeCr_2O_4$) or a Ca-titanate-type (CT-$MgCr_2O_4$) structure. In one high-temperature experiment at 1600 °C, an unquenchable Mg-rich phase with a reconstructed $Mg_4Fe_2^{3+}O_7$ stoichiometry occurred together with $Mg_2(Cr,Fe^{3+})_2O_5$. In one experiment at 1100 °C and 16 GPa with a bulk composition of $Mg_2(Cr_{0.6},Fe_{0.4}^{3+})_2O_5$, an assemblage of O_5 phase + eskolaite–hematite solid solution + periclase was obtained together with minor amounts of the CT-type phase and a β-(Cr,Fe)OOH phase. The occurrence of these two minor phases in this low-temperature experiment is an indicator of variable reaction kinetics amongst the starting materials, which caused chemical heterogeneities to develop at the onset of the experiment.

The structural systematics of $Fe_2^{2+}(Cr,Fe^{3+})_2O_5$ and $(Fe^{2+},Mg)_2(Cr,Fe^{3+})_2O_5$ solid solutions were investigated. It is notable that the Fe^{3+} and Cr endmembers have somewhat different crystal structures, belonging to space groups *Cmcm* (no. 63) and *Pbam* (no. 55), respectively. The phase transition occurs around the midpoint of the Fe^{3+}–Cr joins. In spite of complexities in the behavior of the unit-cell parameters, the variation in molar volume with composition deviates only slightly from linearity.

Wüstite and periclase coexisting in our experiments reveal the incorporation of up to 9 wt % and 25 wt % Cr_2O_3, respectively. This is consistent with the minor Cr contents reported for some ferropericlase inclusions in natural diamond. The limited solubility of other cations in Fe_5O_6 limits the likelihood of it being an accessory phase in the Earth's deep upper mantle and transition zone, except in Fe-rich environments. In contrast, the O_5 phase appears to be more flexible in accommodating a range of divalent and trivalent cations, suggesting that this phase is more likely to be stabilized, potentially where redox reactions related to diamond formation occur.

1 Introduction

Since the report by Chen et al. (2003a, b) of two high-pressure polymorphs of chromite ($FeCr_2O_4$) in the Suizhou shocked meteorite, the phase stabilities of so-called post-spinel phases have taken on a new dimension of importance. This interest has intensified due to the discovery of Fe oxides with a variety of stoichiometries and crystal structures in experiments. The synthesis of $Fe_2^{2+}Fe_2^{3+}O_5$ at high pressures (*Cmcm* space group, Lavina et al., 2011) was followed by the identification of $Fe_3^{2+}Fe_2^{3+}O_6$ (*Cmcm* space group, Woodland et al., 2015; Lavina and Meng, 2015) and the monoclinic-structured phases $Fe_3^{2+}Fe_4^{3+}O_9$ and $Fe_5^{2+}Fe_4^{3+}O_{11}$ (Sinmyo et al., 2016; Ishii et al., 2018). Along with a high-pressure $Fe^{2+}Fe_2^{3+}O_4$ polymorph with a $CaTi_2O_4$ structure (CT-type phase, *Cmcm*) reported earlier by Dubrovinsky et al. (2003), a whole family of post-spinel oxide phases appears to be stable under the pressure and temperature conditions corresponding to the Earth's transition zone and upper portion of the lower mantle. Thus, there is the potential for a range of Fe^{3+}-bearing oxides to become trapped as inclusions in diamond that could serve as indicators of the diamond formation process, as long as their stabilities have been quantified. Likewise, their occurrence in extraterrestrial materials would also allow constraints to be placed on the conditions these materials have undergone, as Chen et al. (2003a, b) aptly demonstrated.

The relevance of such phases to the Earth rests in part on their ability to form solid solutions with other elements in a fashion similar to the spinel or garnet group minerals. For example, magnesiochromite and Cr-rich pyrope are often reported as inclusions in diamonds from certain localities (e.g., Stachel et al., 2003; Stachel and Harris, 2008; Nimis et al., 2019), indicating the potential for Cr to help stabilize major or accessory phases in the deep mantle. The incorporation of Mg has been shown to be possible in many of the phase stoichiometries mentioned above, even if the full extent of cation substitution still remains to be clarified in most cases (Sinmyo et al., 2016; Ishii et al., 2018; Woodland et al., 2013, 2023). Although complete solid solution along the $Fe_2^{2+}Fe_2^{3+}O_5$–$Mg_2Fe_2^{3+}O_5$ binary was reported by Uenver-Thiele et al. (2018), Woodland et al. (2023) found only limited solubility of Mg in $Fe_3^{2+}Fe_2^{3+}O_6$. It should be mentioned that while Mg substitution for Fe^{2+} will increase the $Fe^{3+}/\sum Fe$, substitution of Cr for Fe^{3+} has the opposite effect and acts to lower the $Fe^{3+}/\sum Fe$, providing a mechanism for increasing the range of redox stability of the different oxide phases.

In Cr-bearing compositions, the high-pressure experimental studies of Ishii et al. (2014, 2015) on the post-spinel-phase relations of $FeCr_2O_4$ (Ishii et al., 2014) and $MgCr_2O_4$ (Ishii et al., 2015) have demonstrated the stability of phases with an O_5 stoichiometry (modified ludwigite-type structure, *Pbam*) and a phase of O_4 stoichiometry with a CT-type structure in both endmember systems. For the $FeCr_2O_4$ composition, Ishii et al. (2014) reported an additional high-pressure phase with O_4 stoichiometry and a structure different from but related to the $CaFe_2O_4$-type structure (CF), which they referred to as a "modified $CaFe_2O_4$-type" phase (mCF phase, *Pnma*). This was found to be stable at lower temperatures than where the CT-structured phase was detected.

The high-pressure phase relations of several bulk compositions lying along the $MgCr_2O_4$–$MgSiO_3$ and $MgCr_2O_4$–Mg_2SiO_4 binaries were investigated experimentally by Matrasova et al. (2018) and Sirotkina et al. (2018), respectively. Run products from both of these studies also contained $Mg_2Cr_2O_5$ and the CT-type phase coexisting with a variety of mantle-relevant silicate phases, including wadsleyite, ringwoodite, majoritic garnet and bridgmanite, depending on the pressure and bulk composition employed. In addition, a new phase with a composition $Mg(Mg,Si)(Si,Cr)O_4$ containing ~ 50 mol % Mg_2SiO_4 component was also identified in some experiments at pressures between 12 and 18 GPa (Sirotkina et al., 2018; Bindi et al., 2015).

Although the $Fe_2Cr_2O_5$ and $Mg_2Cr_2O_5$ endmembers are known to be stable between 13 and 16–18 GPa (Ishii et al., 2014, 2015), there are no experimental data currently available for compositions richer in Fe^{2+} or Mg where phases such as $Fe_3^{2+}Cr_2O_6$, $Fe_3^{2+}Cr_4O_9$ and $Fe_5^{2+}Cr_4O_{11}$ or their Mg analogues could be stable. Aside from five experiments reported by Woodland et al. (2013) revealing substantial solid solution between $Fe_2^{2+}Fe_2^{3+}O_5$ and $Fe_2Cr_2O_5$, there is also no information on the stability of Cr–Fe^{3+} solid solutions for any other post-spinel oxide phase. Thus, it is currently unclear if the presence of Cr can act to stabilize one or more of the post-spinel oxides mentioned above as an accessory phase in the mantle assemblage. To address this gap in knowledge, we have investigated phase relations in the Cr–Fe^{2+}–Fe^{3+}–Mg–O system. We initially focus on the stability of $Fe_3Cr_2O_6$ and related compositions containing both Fe^{2+} and Fe^{3+} along with Cr. Then, we investigate the potential stability of $Mg_3Cr_2O_6$ and the phase relations in Mg-bearing bulk compositions containing both Cr and Fe^{3+}.

2 Experimental and analytical methods

Starting materials for experiments with $Fe_3^{2+}Cr_2O_6$ and $Fe_3^{2+}(Cr,Fe^{3+})_2O_6$ bulk compositions were stoichiometric mixtures of pre-synthesized chromite ($FeCr_2O_4$) and Fe_3O_4 along with Fe^0 powder (≤ 60 µm). The combination of magnetite and metal to produce the additional Fe^{2+} necessary for the O_6 stoichiometry avoids the ambiguities inherent in using wüstite, which is always non-stoichiometric. The chromite was synthesized at 1 bar from a mixture of Cr_2O_3 and Fe_2O_3 pressed into pellets and sintered at 1200 °C under reducing conditions of $\log fO_2 = -11.4$ in a vertical tube furnace with a CO–CO_2 gas mixing system. These conditions are appropriate for obtaining single-phase stoichiometric chromite

(Ishii et al., 2014). The pellets were quenched in water and reground and resintered twice in order to assure homogeneity. X-ray powder diffraction patterns revealed a single phase with a unit-cell parameter of $a_o = 8.3775(1)$ Å, which compares well with that reported by Lenaz et al. (2004). Magnetite was similarly produced by reducing Fe_2O_3 at 1300 °C and 1 bar in a 1 : 99 mixture of $CO : CO_2$ ($\log fO_2 = -5.5$), which corresponds to the condition where magnetite is stoichiometric (Dieckmann, 1982). The resulting magnetite had a unit-cell parameter of $a_o = 8.3958(1)$ Å.

For the investigation of $Mg_3Cr_2O_6$ stability, a stoichiometric mixture of pre-synthesized magnesiochromite ($MgCr_2O_4$) along with MgO was used. The $MgCr_2O_4$ was produced from a stoichiometric mixture of MgO and Cr_2O_3 pressed into a pellet. It was initially sintered for 12 d in air at 1100 °C in a box furnace. Then in a final step following the recommendations of Ishii et al. (2015) and O'Neill and Dollase (1994), the material was reground and repressed into a pellet and sintered for 5 h at 1300 °C in a pure CO_2 gas stream in a vertical tube furnace and quenched in water. The result had a very uniform green color. Evaluation of the XRD pattern indicated a single spinel-structured phase with a unit-cell parameter of $a_o = 8.3353(1)$ Å. Starting materials for studying the $Mg_2Cr_2O_5$–$Mg_2Fe^{3+}_2O_5$ binary were prepared by mixing various proportions of pre-synthesized $MgCr_2O_4$ with Fe_2O_3 and MgO to produce the desired stoichiometry.

For the Fe^{2+}–Fe^{3+}-bearing experiments, sample powders were loaded into Ag foil capsules and closed with a hammer. For the Mg-bearing experiments, Pt foil capsules were employed, and for samples containing an additional $Mg_2Fe^{3+}_2O_5$ component, a small amount of PtO_2 powder was added to the capsule before closure in an attempt to maintain the iron in the ferric state during the experiment.

Multi-anvil high-pressure experiments were performed at both the Goethe-Universität Frankfurt and the Bayerisches Geoinstitut, Bayreuth. In Frankfurt, the 800 t Walker-type multi-anvil press was used following the experimental setup and pressure (P) calibration described by Brey et al. (2008). Up to 14 GPa, tungsten carbide anvils with truncated edge lengths of 8 mm were employed along with 14 mm Cr_2O_3-doped MgO octahedra pressure cells. For experiments performed at 18 GPa, the pressure was calibrated using the wadsleyite-to-ringwoodite transformation in Mg_2SiO_4 (1200 °C, 18 GPa; Inoue et al., 2006). Here, the tungsten carbide anvils and MgO octahedra had edge lengths of 4 mm and 10 mm, respectively. At the Bayerisches Geoinstitut two multi-anvil presses were employed up to 23 GPa: the HYMAG MA-6/8 1000 t split-sphere-type press and the Zwick 5000 t press. Cross-calibration between these presses is documented in Keppler and Frost (2005). The pressure cell in Frankfurt employs a Re-foil furnace, whereas a $LaCrO_3$ heater is employed in Bayreuth. W_5 / Re_{95}–W_{26} / Re_{74} thermocouples with the electromotive force uncorrected for pressure were used to monitor the temperature (T). After initial compression, the experiment was heated at a rate of ~ 50 °C min^{-1}. The experiments were terminated by turning off the power and were followed by slow decompression. Uncertainties in pressure and temperature are ± 0.5 GPa and $\pm$ 30–50 °C, respectively (Keppler and Frost, 2005; Brey et al., 2008).

Fragments of the run products from each experiment were mounted in epoxy, ground down and polished in preparation for subsequent investigation by electron microprobe (EPMA). Most of the remaining material was reserved for analysis by X-ray powder diffraction. Microprobe analysis employed a five-spectrometer JEOL JXA-8900 SuperProbe or a JEOL JXA-8530F plus HyperProbe in Frankfurt using pure MgO Fe_2O_3 and Cr_2O_3 as primary standards. The EPMA was operated in wavelength-dispersive mode with an acceleration voltage of 15 kV and a probe current of 20 nA, with various spot sizes from 1–3 µm. The integration time for Fe and Mg was 40 s on the peak, while an integration time of 20 and 40 s on the background was set for Fe and Mg, respectively. For Cr, counting times of 30 s on the peak and 15 s on the background were chosen. A CITZAF algorithm was employed for matrix correction (Armstrong, 1995). Phase homogeneity was verified by performing multiple analyses on single grains and from observing a uniform Z contrast (grey scale) of grains in backscattered electron (BSE) images, which were also used to document sample texture.

Powder X-ray diffraction patterns were obtained at the Institut für Anorganische und Analytische Chemie, Goethe-Universität Frankfurt, using a STOE STADI P diffractometer operating at 45 kV and 35 mA and using monochromatic Mo Kα ($\lambda = 0.70926$ Å) radiation, equipped with a linear PSD or a Mythen detector. Powdered samples were mounted in 0.5 mm diameter glass capillary tubes together with a small amount of silicon that served as an internal standard. The Si powder was cross-calibrated with the NIST LaB_6 standard (NIST 660). Diffraction patterns were collected in transmission mode between 1–100° 2θ. Preliminary phase identification was routinely carried out using CrystalDiffract software from CrystalMaker Software Ltd. (UK). All patterns were then analyzed with the General Structure Analysis System (GSAS; Larson and van Dreele, 1994) software package with the EXPGUI interface of Toby (2001) for phase identification and to determine unit-cell parameters referenced to the Si internal standard.

Sample material from one experiment was also investigated using synchrotron radiation at the Extreme Conditions Beamline P02.2 at PETRA III, Hamburg, Germany, using a PerkinElmer XRD 1621 flat panel detector and a wavelength $\lambda = 0.2907$ Å focused with a KB mirror to a focal spot of $\sim 2 \times 2$ µm^2. The sample-to-detector distance, coordinates of the beam center, tilt angle and tilt plane rotation angle of the detector images were calibrated using a CeO_2 standard. Approximately 30 pieces of the sample material, ranging in size from 10 to 40 µm, were analyzed. Initial diffraction data were collected in wide-scan mode from -20 to $+20$° on the omega

axis. For the 12 fragments that exhibited the best diffraction patterns, XRD data were collected in step-scan mode from −33 to +33° on the omega axis, in 0.5° steps. Every fragment selected for the data collection was an aggregate of single-crystalline domains and was therefore analyzed using a multi-grain approach. The DAFi software program (Aslandukov et al., 2022) was used to identify groups of reflections attributable to the same crystals, and the identified orientation matrices were then used in the CrysAlisPro software (CrysAlisPro, 2019) to integrate the single-crystal XRD data for each crystalline domain in order to obtain accurate unit-cell parameters.

3 Results and discussion

We first present results from experiments with Mg-free compositions, and data are reported in Tables 1 and 2, with the latter containing the compositions and unit cells for the recovered high-pressure oxide phases. This is followed by the results from experiments with Mg-bearing starting compositions presented in an analogous way in Tables 3 and 4.

3.1 The Cr–Fe^{2+}–Fe^{3+}–O subsystem

Stability of $Fe_3Cr_2O_6$. A series of experiments between 14 and 20 GPa and 1200–1500 °C was undertaken to ascertain whether the $Fe_3Cr_2O_6$ endmember has a stability field or not. This range was chosen based on the conditions (i) in which chromite ($FeCr_2O_4$) breaks down according to Ishii et al. (2014) and (ii) where Fe_5O_6 is known to be stable (Woodland et al., 2023). As it turns out, the $Fe_3Cr_2O_6$ endmember phase was not found in any of our experiments (Table 1). At the lowest pressure of 14 GPa (and 1200 °C), chromite coexists with wüstite. Otherwise, $Fe_2Cr_2O_5$ with the modified ludwigite-type structure occurs in the experimental products together with wüstite (Fig. 1a). This assemblage also implies that no other high-pressure phases with stoichiometries between $Fe_2Cr_2O_5$ and wüstite are stable over the broad range of P–T conditions of our experiments (i.e., $Fe_3^{2+}Cr_2O_6$, $Fe_5^{2+}Cr_4O_{11}$).

Phase relations. The assemblage $Fe_2Cr_2O_5$+ wüstite is stable over a wide range of P and T. However, in two experiments, one each at 18 and 20 GPa, small amounts of additional $FeCr_2O_4$ with a modified Ca-ferrite-type structure (mCF) were detected by XRD (Table 1). It is notable that this phase appeared in experiments run at relatively low temperatures, so while reaction clearly occurred, it may be that the entire sample may not be completely equilibrated. However, the occurrence is consistent with the P–T stability of this phase reported by Ishii et al. (2014). On the other hand, the CT-type polymorph of $FeCr_2O_4$ found by Ishii et al. (2014) at higher temperatures ($T \geq 1400$ °C) was not detected in our experiments. The persistence of $Fe_2^{2+}Cr_2O_5$ at high pressure compared to the experiments of Ishii et al. (2014) can be attributed to our bulk compositions being richer in Fe. Ishii et al. (2014) investigated the $FeCr_2O_4$ composition and had Cr_2O_3 coexisting with $Fe_2^{2+}Cr_2O_5$, whereas wüstite was present in our experiments using an $Fe_3Cr_2O_6$ bulk composition. Thus, it is likely that the P–T stability of $Fe_2Cr_2O_5$ is somewhat different when it coexists with wüstite compared with Cr_2O_3, in a manner similar to that observed for Fe_4O_5 depending on whether it coexists with Fe_2O_3 or not (Myhill et al., 2016).

Although the presence of three phases in two samples of the Fe^{2+}–Cr endmember composition would appear to violate the phase rule for phase equilibrium, textures of the two samples containing the mCF-type phase reveal that $Fe_2Cr_2O_5$ always occurs in between this phase and wüstite (Fig. 1b). Thus, two local equilibria were established during the experiment with $Fe_2Cr_2O_5$ in equilibrium with wüstite and $Fe_2Cr_2O_5$ also being locally in equilibrium with the mCF-type phase. Such small-scale heterogeneities may have been induced by the different starting materials, chromite, magnetite and Fe^0 reacting at different rates at the beginning of the experiment. For example, magnetite has been observed to break down quite rapidly in in situ experiments (e.g., Schollenbruch et al., 2011; Woodland et al., 2012). If this occurs more rapidly than for chromite, isolated Cr-rich domains might develop that could subsequently transform into the mCF-type phase (but see below) and then take a long time to homogenize. As mentioned previously, the mCF-type phase only occurs in experiments performed at ≤ 1300 °C (Table 1).

A further explanation for the additional mCF-type phase can be related to a small amount of oxidation that apparently occurred during the experiments, producing a small amount of Fe^{3+}. In fact, microprobe analysis reveals that the O_5 phase always has a small deficit in Cr content, which corresponds to the presence of 10–20 mol % $Fe_2^{2+}Fe_2^{3+}O_5$ component (Table 2). This is even the case for sample H5743, where a small excess of metallic Fe was added to the starting mix in an attempt to suppress oxidation during the experiment (Table 1). Thus, the presence of Fe^{3+} shifts the bulk composition off of the intended $Fe^{2+}O$–$CrO_{1.5}$ join and slightly into the $Fe^{2+}O$–$CrO_{1.5}$–$Fe^{3+}O_{1.5}$ ternary system. It is notable that Fe^{3+} preferentially partitions into the O_5 phase compared to the coexisting mCF phase (Table 2). The presence of Fe^{3+} may also explain why the O_5 phase is still stable in our two experiments at 20 GPa and 1400 and 1500 °C (Table 1) in contrast to the CT-type polymorph of $FeCr_2O_4$ found by Ishii et al. (2014) in these conditions.

It must be mentioned here that in their comparison of results from quench and in situ experiments with the $FeCr_2O_4$ endmember composition, Ishii et al. (2014) demonstrated that the mCF phase actually had the Ca-ferrite (CF) structure (*Pnma*, Decker and Kasper, 1957) at high pressures and temperatures and that it had converted to the mCF-type structure in their quench experiments during decompression. This is most likely the case in our quench experiments as well, so we consider that the high P–T phase relations described above

Table 1. Conditions and run products of experiments in the Cr_2O_3–FeO ± Fe_2O_3 system along with refined cell parameters and Cr content of periclase and spinel.

Experiment	Starting stoichiometry	Pressure [GPa]	Temperature [°C]	Duration [h]	Run products[1]	Wüstite unit cell [Å]	nCr[2]	Cation sum[2]	Cr-spinel unit cell [Å]	nCr
	XCr									
$Fe_3Cr_2O_6$										
M847	1	14	1400	2	sp + wü	4.3025(2)	0.114(4)	0.943(2)	8.3839(1)	1.828(6)
Z2262	1	16	1500	1.5	O5L + (sp)				8.3841(5)	1.732(14)
M851	1	18	1200	2	O5L + wü + (CF)	4.3144(2)	0.059(4)	0.971(2)		
M849	1	18	1500	2	O5L + wü	4.3100(7)	0.077(2)	0.9614(10)		
H5696	1	20	1300	2.25	O5L + wü + (CF)	4.3153(2)	0.059(7)	0.971(4)		
H5743[3]	1	20	1400	2	O5L + wü	4.3073(3)	0.1079(13)	0.9457(9)		
H5699	1	22	1500	1	O5L + wü	4.3102(4)	0.079(16)	0.9607(8)		
$Fe_3(Fe,Cr)_2O_6$										
M865	0.65	14	1400	2	O5L + wü	4.2820(1)	0.110(4)	0.945(2)		
Z2262_60–40	0.4	16	1500	1.5	O5C + wü	4.2834(1)	0.0824(9)	0.9588(4)		
Z2263_60–40	0.4	16	1500	1.5	O5C + wü	4.2945(1)	0.0487(13)	0.9756(7)		
M853	0.2	12	1400	2	O5C + wü	4.2804(1)	0.028(2)	0.986(9)		
M859	0.2	14	1400	2	O5C + wü	4.2791(1)	0.0318(8)	0.9841(4)		
Z2263_80–20	0.2	16	1500	1.5	O5C + wü	4.2920(1)	0.0267(11)	0.9866(5)		
M861	0.05	11	1350	2	O6 + O5C + wü	4.2607(1)	0.0121(4)	0.9939(2)		
M854	0.05	14	1400	2	O6 + wü	4.2654(1)	0.0137(1)	0.9931(1)		
H5742	0.05	20	1400	2	O6 + O5C					

[1] sp, spinel; wü, wüstite; O5L, phase with O5 stoichiometry and modified ludwigite structure; CF, O4 stoichiometry with Ca-ferrite structure; O5C, phase with O5 stoichiometry and *Cmcm* structure; () indicates trace quantities detected by XRD. [2] Number of cations calculated on a one-oxygen basis. [3] Excess metallic Fe° added.

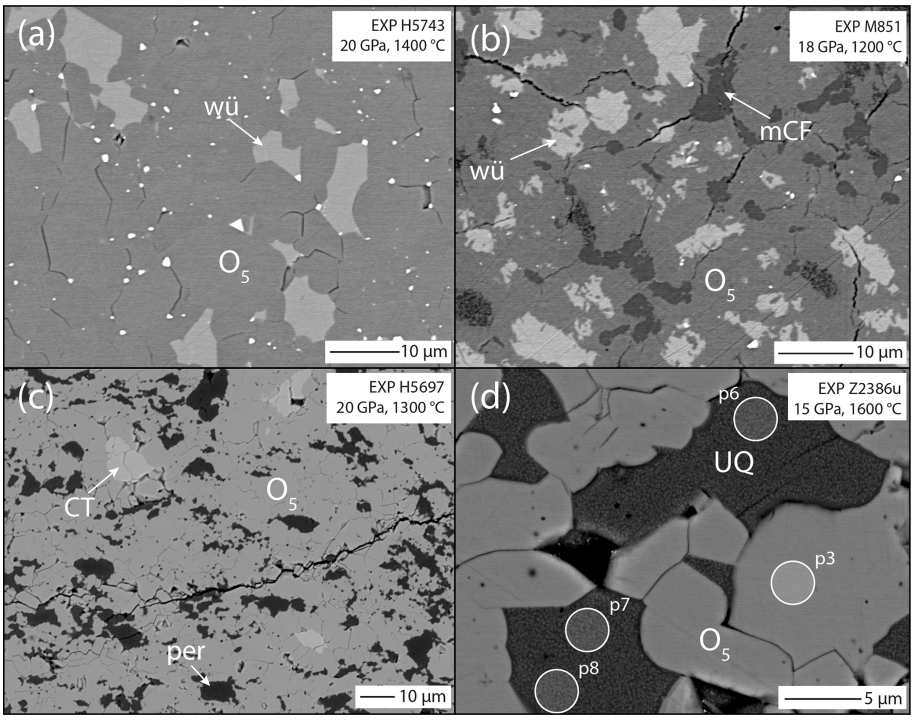

Figure 1. Backscattered electron images of run products from selected experiments: **(a)** texture of sample H5743 indicating $Fe_2Cr_2O_5$ (medium grey) coexisting with wüstite (bright) and **(b)** sample M851 illustrating the presence of three phases, $Fe_2(Cr,Fe)_2O_5$ (medium grey), wüstite (bright) and mCF-$Fe(Cr,Fe)_2O_4$ (dark); note that the mCF-type phase is never in direct contact with wüstite. Also note that some of the mCF-type phase has reacted during the quench. The tiny very bright grains are apparently unreacted Fe metal from the starting material. **(c)** The Mg-bearing sample H5697 comprising O_5 and periclase with traces of CT-type $MgCr_2O_4$; **(d)** texture of the Mg-bearing sample Z2386u illustrating the coexistence of the O_5 phase with the modified ludwigite structure and an unquenchable phase that has exsolved into periclase (medium grey) and spinel (bright). Large-diameter (3 µm) analysis spots indicated in the image yield a bulk composition consistent with $(Mg_{3.93},Fe^{2+}_{0.07})(Cr_{1.11},Fe^{3+}_{0.89})O_7$ stoichiometry.

actually relate to an O_4 phase with the CF-type structure. From microprobe imaging, we find no evidence of changes in composition having occurred through the CF-type to mCF-type structural adjustment during decompression. In fact, this is unlikely, since decompression of an experiment is at room temperature, where solid-state diffusion is very slow. However, the relative instability of the O_4 phase is also apparent by partial breakdown textures apparent in BSE images (Fig. 1b) that formed during the quench rather than during decompression. In this context, solid solution with Fe^{3+} is also not expected to help to stabilize the crystal structure since hp-Fe_3O_4 has never been observed under ambient conditions, reverting to magnetite during decompression (e.g., Fei et al., 1999; Dubrovinsky et al., 2003; Uenver-Thiele et al., 2024).

Having demonstrated that the $Fe^{2+}_3Cr_2O_6$ endmember composition does not appear to be stable, we undertook a further series of experiments with bulk compositions along the $Fe^{2+}_3Fe^{3+}_2O_6$–$Fe^{2+}_3Cr_2O_6$ binary join to ascertain the extent of Cr substitution possible in Fe_5O_6 (Tables 1, 2). For most of the compositional range, O_5 + wüstite is the stable assemblage. Only at a low $Fe^{2+}_3Cr_2O_6$ content of 5 mol% in the starting material did an O_6-structured phase appear in the run products, indicating that only very limited amounts of Cr can be incorporated into the Fe_5O_6 (∼0.12 cations Cr per formula unit, c.p.f.u.). In contrast, we observe complete Cr–Fe^{3+} solid solution in the O_5 phase. What makes this even more remarkable is that the two endmembers of this binary series, $Fe^{2+}_2Fe^{3+}_2O_5$ and $Fe_2Cr_2O_5$, have somewhat different crystal structures (*Cmcm*, no. 63, and *Pbam*, no. 55, respectively; see below).

3.2 The Cr–Mg–Fe^{2+}–Fe^{3+}–O system: the addition of Mg

Analogous to the Fe subsystem, we initially investigated the stability of the $Mg_3Cr_2O_6$ endmember composition over a pressure range of 14–20 GPa at temperatures between 1200 and 1500 °C (Table 3). The originally anticipated O_6 phase was not observed under these conditions. Instead, the assemblage $Mg_2Cr_2O_5$+MgO was always stable. At 20 GPa, traces of $MgCr_2O_4$ with the CT-type structure also appeared (Fig. 1c), consistent with the work of Ishii et al. (2015). Not only does the assemblage $Mg_2Cr_2O_5$+MgO in our experi-

Table 2. Composition and refined unit-cell parameters of phases in run products from experiments in the Cr_2O_3–FeO± Fe_2O_3 system.

Experiment	Phase	nCr	nFe^{2+}	nFe^{3+}	Unit-cell parameters				
		c.p.f.u.	c.p.f.u.	c.p.f.u.	a [Å]	b [Å]	c [Å]	V [Å^3]	Mol vol [cm^{3}mol^{-1}]
$Fe_2(Cr,Fe)_2O_5$									
Z2262	O5L	1.641(6)	2	0.359(6)	9.6893(3)	12.5189(3)	2.9056(1)	352.445(10)	53.061(2)
M851	O5L	1.78(8)	2	0.21(8)	9.6899(5)	12.4927(6)	2.9078(1)	352.00(2)	52.993(3)
M849	O5L	1.63(2)	2	0.37(2)	9.6874(5)	12.5015(6)	2.9071(1)	352.07(2)	53.004(3)
H5696	O5L	1.74(6)	2	0.26(6)	9.6871(10)	12.4951(11)	2.9072(2)	351.89(3)	52.977(5)
H5743	O5L	1.691(6)	2	0.309(6)	9.6870(3)	12.5169(3)	2.9077(1)	352.566(9)	53.079(2)
H5699	O5L	1.68(3)	2	0.32(3)	9.6872(3)	12.5105(3)	2.9070(1)	352.298(10)	53.038(2)
M865	O5C	1.283(14)	2	0.716(14)	9.7088(3)	12.5308(3)	2.9035(1)	353.241(10)	53.180(2)
Z2262_60–40	O5C	0.933(6)	2	1.067(5)	2.9068(1)	9.7359(3)	12.5274(4)	354.533(13)	53.375(2)
Z2263_60–40	O5C	0.95(2)	2	1.05(2)	2.9041(1)	9.7440(2)	12.5375(2)	354.778(8)	53.412(1)
M853	O5C	0.43(3)	2	1.57(3)	2.8991(1)	9.7665(2)	12.5554(3)	355.491(10)	53.519(2)
M859	O5C	0.41(2)	2	1.59(2)	2.8995(1)	9.7673(2)	12.5588(3)	355.671(10)	53.546(2)
Z2263_80–20	O5C	0.42(2)	2	1.58(2)	2.8996(1)	9.7653(2)	12.5560(2)	355.526(9)	53.524(2)
M861	O5C	0.093(11)	2	1.907/11)	2.8932(1)	9.7936(4)	12.5694(4)	356.155(14)	53.619(2)
H5742	O5C	0.060(2)	2	1.940(2)	2.8950(1)	9.7895(4)	12.5632(4)	356.051(13)	53.603(2)
$Fe_3(Fe,Cr)_2O_6$									
M861		0.087(1)	3	1.913(1)	2.8826(7)	9.922(3)	15.359(3)	439.27(10)	66.132(15)
M854		0.11(5)	3	1.89(5)	2.8879(1)	9.9294(2)	15.3560(3)	440.339(12)	66.293(2)
H5742		0.12(1)	3	1.88(1)	2.8869(3)	9.9243(10)	15.3491(13)	439.76(4)	66.206(6)
$Fe(Cr,Fe)_2O_4$									
M851	mCF	1.94(1)	1	0.06(1)	9.066(2)	2.9575(6)	10.642(3)	285.32(8)	42.955(15)
H5696	mCF	1.99(4)	1	0.01(4)	9.067(7)	2.9595(17)	10.657(8)	285.96(25)	43.05(4)

[1]O5L, phase with a modified ludwigite (*Pbam*) structure; O5C, phase with a Ca-ferrite (*Cmcm*) structure; mCF, modified Ca-ferrite structure.

mental run products indicate the instability of $Mg_3Cr_2O_6$, but it also means that no additional phases with Mg-rich compositions lying between $Mg_2Cr_2O_5$ and periclase can be stable either. As with the Fe^{2+} endmember, we find that $Mg_2Cr_2O_5$ remains stable at higher pressures than those reported by Ishii et al. (2015) in their study of $MgCr_2O_4$ phase relations (e.g., at 20 GPa, Table 3). Again, this demonstrates that the P–T stability field of $Mg_2Cr_2O_5$ is influenced by whether it coexists with eskolaite (Cr_2O_3) or periclase.

Since the $Mg_3Fe_2^{3+}O_6$ endmember is already known not to be stable (Woodland et al., 2023), it was instead decided to perform four experiments to investigate relations along the $Mg_2Cr_2O_5$–$Mg_2Fe_2^{3+}O_5$ binary to check if solid solution is complete (Table 3). These experiments were performed at 14–16 GPa and a range of temperatures from 1100 to 1600 °C (Table 3). In all cases, the run products were dominated by the O_5 phase, with three samples also containing coexisting periclase (Table 3). No O_6-structured phase was detected. The range in composition of the O_5 phase seems to indicate that Cr–Fe^{3+} substitution is complete across the $Mg_2Cr_2O_5$–$Mg_2Fe_2^{3+}O_5$ join. We note that in spite of adding a small amount of PtO_2 to the samples to help to maintain a high oxidation state, a little reduction appears to have occurred during these experiments, as revealed by the presence of Fe^{2+} when calculating phase stoichiometries from microprobe analyses (Tables 3, 4).

In the highest-temperature experiment (Z2386u), instead of the O_5 phase coexisting with periclase, another phase appeared that has an exsolved texture, indicating that it did not survive quenching from high P and T (Fig. 1d). Such textures have also been observed in the Cr-free $MgFe_2O_4$ system (Uenver-Thiele et al., 2017a). Microprobe analyses using a defocused electron beam of 3 µm diameter (Fig. 1d) yielded results consistent with a $(Mg_{3.93},Fe^{2+}_{0.07})(Cr_{1.11},Fe^{3+}_{0.89})O_7$ stoichiometry. An unquenchable Mg-rich phase with $Mg_4Fe_2^{3+}O_7$ stoichiometry has already been proposed by Uenver-Thiele et al. (2017a) and Woodland et al. (2023). If our interpretation is correct, the results of experiment Z2386u would indicate that Cr can be readily incorporated into this phase; unfortunately the presence of Cr did not help to stabilize the phase to the point where it could survive quenching. Comparison of the reconstructed O_7 composition with the coexisting O_5 phase (Table 4) does indicate that Cr is somewhat favored by the O_5 phase ($X_{Cr} = 0.55$ in O_7 phase vs. $X_{Cr} = 0.63$ in the O_5 phase, where $X_{Cr} = nCr / (nCr + nFe^{3+})$), consistent with the presence of Fe^{3+} serving to stabilize the O_7 phase at the high temperature of this experiment.

https://doi.org/10.5194/ejm-36-845-2024

Table 3. Conditions and run products of experiments in the Cr_2O_3–MgO ± Fe_2O_3 ± FeO system and refined unit-cell parameters and Cr content of spinel and periclase.

Experiment	Starting stoichiometry XCr	Pressure [GPa]	Temperature [°C]	Duration [h]	Run products[1]	Periclase unit cell [Å]	nCr[2]	nFe[2]	Cation sum[2]	Cr-spinel unit cell [Å]	nCr
$Mg_3Cr_2O_6$											
M848	1	14	1400	3	sp + O5L + per	4.1980(1)	0.1314		0.9343	8.3341(1)	
M852	1	18	1200	4	O5L + per	4.2083(1)	0.0112		0.9944		
M850	1	18	1400	2	O5L + per	4.1989(1)	0.0772		0.9614		
H5697Mg	1	20	1300	2	O5L + per + (CT)	4.2068(1)	0.0454		0.9773		
H5698Mg	1	20	1500	2	O5L + per + (CT?)	4.2036(1)	0.0577		0.9712		
$Mg_2(Fe,Cr)_2O_5$											
M855[3]	0.8	14	1400	4	O5L + sp + per	4.1928(1)	0.156(2)	0.066(1)	0.9218(10)	8.3483(1)	1.67(2)
Z2281u[3]	0.6	16	1100	3	O5L + hem + per + CT + (Cr,Fe)OOH	4.2160(1)	0.008(3)	0.033(5)	0.9959(13)		
Z2386u[3]	0.5	15	1600	1.5	O5L + UQ + [per] + mgs	4.1832(2)					
M863[3]	0.2	14	1500	1	O5C + per + (hem) + (sp)	4.1960(2)	0.0475(4)	0.2029(4)	0.9763(2)	8.3798(6)	

[1] per, periclase; CT, O_4 stoichiometry with a Ca-titanate structure; hem, Fe_2O_3–Cr_2O_3 solid solution; O5L, phase with O_5 stoichiometry and a modified ludwigite structure; O5C, phase with O_5 stoichiometry and *Cmcm* structure; mgs, magnesite; UQ, unquenchable phase; () indicates trace quantities detected by XRD and quench phase detected by XRD. [2] Cations calculated on a one-oxygen basis. [3] Experiment with a small amount of PtO_2 added.

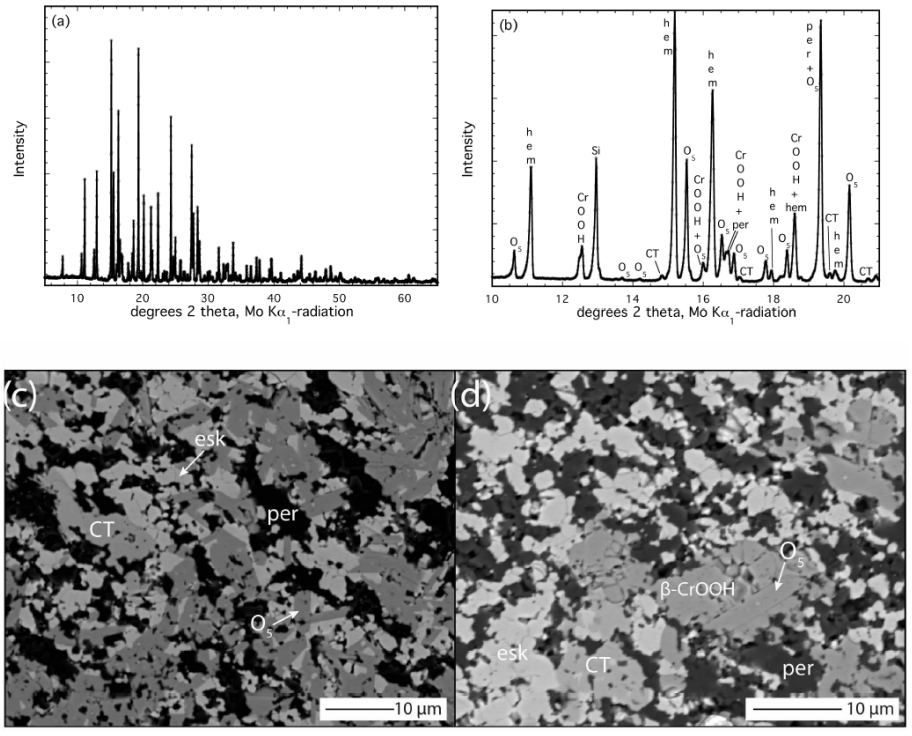

Figure 2. Analysis of the run products from experiment Z2281u. **(a)** Powder XRD pattern; **(b)** inset of powder XRD pattern between 10 and 21° 2θ. **(c)** BSE image of run products containing eskolaite–hematite solid solution (bright), periclase (dark), the O_5 phase (medium grey) and a crystal of the CT-type phase (slightly lighter grey). **(d)** BSE image illustrating the occurrence of β-CrOOH along with O_5, eskolaite–hematite (bright), the CT-type phase (slightly brighter than O_5) and periclase (dark).

The run products of the lowest-temperature experiment at 1100 °C and 16 GPa (Z2281) contain a total of five phases that were detected first by XRD and then by a microprobe (Table 3, Fig. 2a, b, c, d). The dominant phases are the O_5 phase coexisting with an eskolaite–hematite solid solution and periclase in subequal quantities, as given by a refinement with GSAS. The occurrence of these three phases can be understood by comparing the phase diagrams presented by Ishii et al. (2015) and Uenver-Thiele et al. (2017a) for the $MgCr_2O_4$ and $MgFe_2O_4$ endmember compositions, respectively. The P–T conditions of our experiment already lie close to the boundary separating the stability fields of $Cr_2O_3 + MgO$ and $Mg_2Cr_2O_5 + Cr_2O_3$, and the addition of Fe^{3+} should expand the two-oxide stability field to higher P and T so that the occurrence of these three phases is not surprising for a bulk composition near the middle of the $Mg_2Cr_2O_5$–$Mg_2Fe_2^{3+}O_5$ join (Table 3). However, additional low-intensity peaks were detected in the XRD pattern (Fig. 2a, b). A number of peaks are consistent with the CT-type polymorph of $MgCr_2O_4$, and others seem to fit the β-CrOOH phase with the space group $Pmn2_1$. Although the latter phase seems unlikely due to the fact that no H_2O was added to the experiment, an analogous occurrence of phase B in a nominally non-hydrous experiment was recently reported by Uenver-Thiele et al. (2018) and attributed to adsorbed water on the extremely fine-grained PtO_2 powder that was added to maintain a high oxidation state. This is likely the same case here. Presumably this hydrous phase formed by reaction between newly formed eskolaite (from the apparently rapid breakdown of $MgCr_2O_4$ in the starting material) and the trace volatile phase locally present in the sample.

To verify the presence of these two minor phases, sample material was further investigated using synchrotron radiation and applying the multi-grain single-crystal XRD approach. The unit cells obtained from indexing the diffraction patterns indicated the presence of the following phases: $(Mg,Cr,Fe)_4O_5$, $(Cr,Fe)_2O_3$, β-(Cr,Fe)OOH and CT-type $(Mg,Fe)(Cr,Fe)_2O_4$. No single-crystal grains belonging to periclase were found. This is probably due to its small unit-cell volume, which generally creates problems while using the DAFi algorithm. While the d spacings corresponding to periclase can be found in powder XRD patterns, it should be noted that many of the reflections overlap with those from $(Mg,Cr,Fe)_4O_5$ and/or β-(Cr,Fe)OOH.

Further EPMA analysis also revealed grains with stoichiometric compositions consistent with the CT phase and β-(Cr,Fe)OOH, with the latter yielding oxide totals of $\sim$ 85 wt % (Table 4; Fig. 2d). Identification of this phase in BSE images is difficult since it essentially has the same grey scale as the O_5 phase (Fig. 2d). The appearance of the CT-

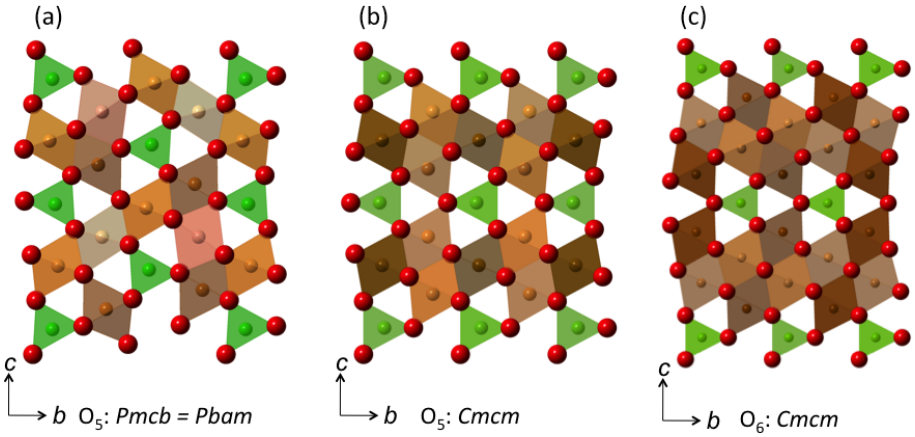

Figure 3. Crystal structures of **(a)** the O_5 phase with the modified ludwigite structure (*Pbam*; Ishii et al., 2015) here set to the equivalent space group *Pmcb* in order to afford direct comparison with **(b)** the O_5 phase with the *Cmcm* structure (Boffa Ballaran et al., 2015). The structure of the related O_6 phase with the *Cmcm* structure is depicted in **(c)**, from Lavina and Meng (2015). In all structures, the prismatic sites are depicted in green, while the crystallographically distinct octahedral sites are portrayed in different shades of brown.

type phase (Fig. 2c, d) is interesting since the stability field of this phase in the $MgCr_2O_4$ endmember lies at significantly higher pressure, and the post-spinel $MgFe_2O_4$ phase has a different crystal structure (Ishii et al., 2015; Uenver-Thiele et al., 2017b). The occurrence of both of these minor phases in this low-T experiment is an indicator of variable reaction kinetics amongst the starting materials, which caused chemical heterogeneities to develop locally and subsequently established local equilibria within the sample (not to mention trace contamination of adsorbed H_2O).

In terms of composition, the O_5 phase is richer in Cr ($X_{Cr} = 0.75(4)$), and the eskolaite–hematite solid solution is somewhat poorer in Cr ($X_{Cr} = 0.52(5)$) than the bulk starting material ($X_{Cr} = 0.6$) (see Table 4), indicating that Cr partitions preferentially into the O_5 phase compared to the rhombohedral-structured phase. In contrast, the rare CT-type phase has an $X_{Cr} = 0.58(5)$, essentially equal to the initial bulk composition. Stoichiometric calculations reveal a small amount of Fe^{2+} to be present in these phases, indicating minor reduction during the experiment. The β-CrOOH phase contains the most Cr ($X_{Cr} = 0.82(4)$), which agrees with the results of the single-crystal refinement.

3.3 Structural systematics of $Fe_2^{2+}(Cr,Fe^{3+})_2O_5$ and $(Fe^{2+},Mg)_2(Cr,Fe^{3+})_2O_5$ solid solutions

Since the O_5 phase appeared in nearly all our experimental run products, we can combine our results with literature data to assess the structural changes related to $Cr–Fe^{3+}$ substitution in Fe^{2+}- and Mg-bearing compositions of this phase. The compositional range of the O_5 phase obtained in our different experiments indicates that solid solution is complete across the respective binaries and presumably also for more complex $(Fe^{2+},Mg)_2(Cr,Fe^{3+})_2O_5$ compositions. From the start, it is important to note that the Fe^{3+} and Cr endmember compositions have somewhat different crystal structures, with Fe^{3+} and Cr endmembers belonging to space groups *Cmcm* (no. 63) and *Pbam* (no. 55), respectively (Lavina et al., 2011; Boffa Ballaran et al., 2015; Ishii et al., 2014, 2015). In the Fe^{2+}-bearing system, it is apparent that the transition between the *Cmcm* and *Pbam* structure types must occur at $\sim 50\%$ Fe_4O_5 – 50 % $Fe_2Cr_2O_5$ (Table 2; *Cmcm* to $X_{Cr} = 0.47$; *Pbam* from $X_{Cr} = 0.64$). Both structures have similar unit-cell parameters of approximately 2.9, 9.7 and 12.5 Å, although the chosen crystallographic directions are different (e.g., see Table 2). Therefore, in order to compare the two crystal structures we have transformed the *Pbam* space group into the *Pmcb* setting so that the unit-cell parameters are as follows: a (*Cmcm*), a (*Pmcb*) = c (*Pbam*), b (*Cmcm*), b (*Pmcb*) = a (*Pbam*) and c (*Cmcm*), and c (*Pmcb*) = b (*Pbam*). The two structure types are composed of the same types of polyhedral (Fig. 3a, b). In the *Cmcm* structure, layers of edge-sharing octahedra alternate with layers of bi-capped triangular prisms, which are stacked in the c direction (Fig. 3b; Boffa Ballaran et al., 2015). In the *Pmcb* structure, the edge-sharing octahedra have a zig-zag configuration with triangular prisms in between that also stack along the c axis (Fig. 3a, b axis in the *Pbam* space group) as first described by Enomoto et al. (2009).

The variation in the unit-cell parameters with composition is illustrated in Fig. 4a, b and c. The intermediate-length b parameter (a parameter in *Pbam*) exhibits the largest change, decreasing by ~ 0.14 Å with increasing Cr content across the join (Fig. 4b). The variation is close to linear with composition. This direction is along the edge-sharing layers of the octahedra, where Cr and Fe^{3+} are expected to reside (Fig. 3a, b; Ishii et al., 2014; Boffa Ballaran et al., 2015) so that substitution of the smaller Cr cation for Fe^{3+} (Cr = 0.615 Å vs. Fe^{3+} = 0.645 Å, Shannon et al., 1976) into these sites would be expected to lead to shortening. However, the linear be-

Table 4. Composition and refined unit-cell parameters of phases in run products from experiments in the Cr_2O_3–$MgO \pm Fe_2O_3 \pm FeO$ system.

Experiment	Phase	nCr	nMg	nFe^{2+}	nFe^{3+}	Unit-cell parameters				
		c.p.f.u.	c.p.f.u.	c.p.f.u.	c.p.f.u.	a [Å]	b [Å]	c [Å]	V [Å^3]	Mol vol [cm^3]
$Mg_2(Fe,Cr)_2O_5$										
M848	O5L[1]	2	2			9.6085(5)	12.4361(5)	2.8495(1)	340.49(2)	51.261(2)
M852	O5L	2	2			9.6068(4)	12.4253(4)	2.8506(1)	340.272(13)	51.228(2)
M850	O5L	2	2			9.6074(2)	12.4361(2)	2.8498(1)	340.493(7)	51.261(1)
H5697Mg	O5L	2	2			9.6067(3)	12.4345(3)	2.8495(1)	340.389(9)	51.246(2)
H5698Mg	O5L	2	2			9.6085(2)	12.4344(2)	2.8499(1)	340.49(6)	51.261(1)
M855[2]	O5L	1.671(5)	1.897(4)	0.102(4)	0.329(6)	9.6299(3)	12.4594(4)	2.8582(1)	342.932(13)	51.628(2)
Z2281u[2]	O5L	1.50(9)	1.76(7)	0.24(7)	0.50(9)	9.6474(5)	12.4786(6)	2.8646(1)	344.86(2)	51.919(2)
Z2386u[2]	O5L	1.26(2)	1.916(3)	0.084(3)	0.74(2)	9.6498(2)	12.4851(3)	2.86411(1)	345.059(10)	51.949(2)
M863[2]	O5C	0.42(8)	1.858(5)	0.142(5)	1.58(8)	2.8807(1)	9.6966(3)	12.516(3)	349.606(10)	52.633(2)
$Mg(Fe,Cr)_2O_4$										
H5697Mg	CT	2	1			2.850(3)	9.505(11)	9.672(8)	261.97(28)	39.44(4)
Z2281u	CT	1.15(11)	0.83(2)	0.17(2)	0.85(11)	2.866(2)	9.546(7)	9.749(6)	266.8(2)	40.17(3)
$(Fe,Cr)_2O_3$										
Z2281u		1.05(11)	0.03(2)	0.92(11)		5.0036(1)	5.0036(1)	13.6238(4)	295.390(9)	29.647(1)
(Cr,Fe)OOH										
Z2281u		0.82(4)	0.03(2)		0.14(1)	2.9744(7)	4.333(2)	4.8846(12)	62.95(4)	18.95(2)

[1] O5L, phase with a modified ludwigite (*Pbam*) structure; O5C, phase with a Ca-ferrite (*Cmcm*) structure; CT, O4 phase with a Ca-titanate structure. [2] Experiment with a small amount of PtO_2 added.

havior is remarkable considering the rearrangement in the crystal structure that occurs in the middle of the binary join. The longer c parameter (b parameter in *Pbam*) also decreases with increasing Cr substitution but to a much lesser extent than observed for the b parameter (~ 0.08 Å, Fig. 4c). This parameter varies roughly linearly but not with respect to the two endmembers, and there is increased scatter in Cr-rich compositions with the *Pbam* structure type. The scatter may be due to the fact that many *hkl* reflections directly related to the long cell edge (b in *Pbam*) have either very low intensities (i.e., 020 in *Pbam*) or overlap with the Si standard (040 in *Pbam*) or other reflections from the O_5 phase itself (060 and 080 in *Pbam*), making refinement of this parameter less well constrained. On the other hand, results for the six samples with $X_{Cr} = 0.89$–0.82 suggest a correlation between the b parameter and the temperature of the experiment (Tables 1, 2). This would imply that some cation disorder was at least partially preserved upon quenching the experiment from high temperature. Considering that the prismatic sites are expected to remain essentially occupied by Fe^{2+} across the join (Ishii et al., 2014; Boffa Ballaran et al., 2015), it may be expected that Fe^{3+} and Cr will exhibit particular site preferences between the adjacent octahedral sites. In fact, the combination of accommodating the smaller Cr cation and the subsequent disorder that results is probably the cause for the buckling of the layers in the *Cmcm* structure type, leading to the transition to the *Pbam* structure type with its zig-zag configuration and two additional crystallographically distinct octahedral sites (compare Fig. 3a and b).

The behavior of the shortest parameter (a parameter in *Cmcm*, c parameter in *Pbam*) in the solid solutions is a further indication of complicated interactions due to cation substitution. This cell parameter exhibits a small increase in its length with addition of Cr. A linear relationship exists for the *Cmcm* polysome, but then the value of this parameter levels off in Cr-richer compositions where the *Pbam* structure type is stable (Fig. 4a). An increase in cell length, even small (~ 0.01 Å), is unexpected for substitution of a smaller cation. It is even more surprising considering that this crystallographic direction is mostly controlled by the height of the prismatic site. In fact, such behavior is not observed in Mg-bearing compositions (see below). This suggests that the systematics observed in Fig. 4a are related to electron hopping between Fe^{2+} and Fe^{3+} involving the prismatic site, yielding an average charge of $Fe^{2.5+}$, which should have a smaller ionic radius than Fe^{2+}. The addition of Cr reduces the number of nearest neighbors that can participate in electron hopping so that the formal charge of the Fe occupying the prismatic site becomes 2+ once a particular compositional threshold is reached. This threshold appears to coincide with the phase transition from *Cmcm* to *Pbam* in the middle of the join also as the amount of formal Fe^{3+} available for charge transfer has decreased significantly. Note that the short c parameter reported by Ishii et al. (2014) for the

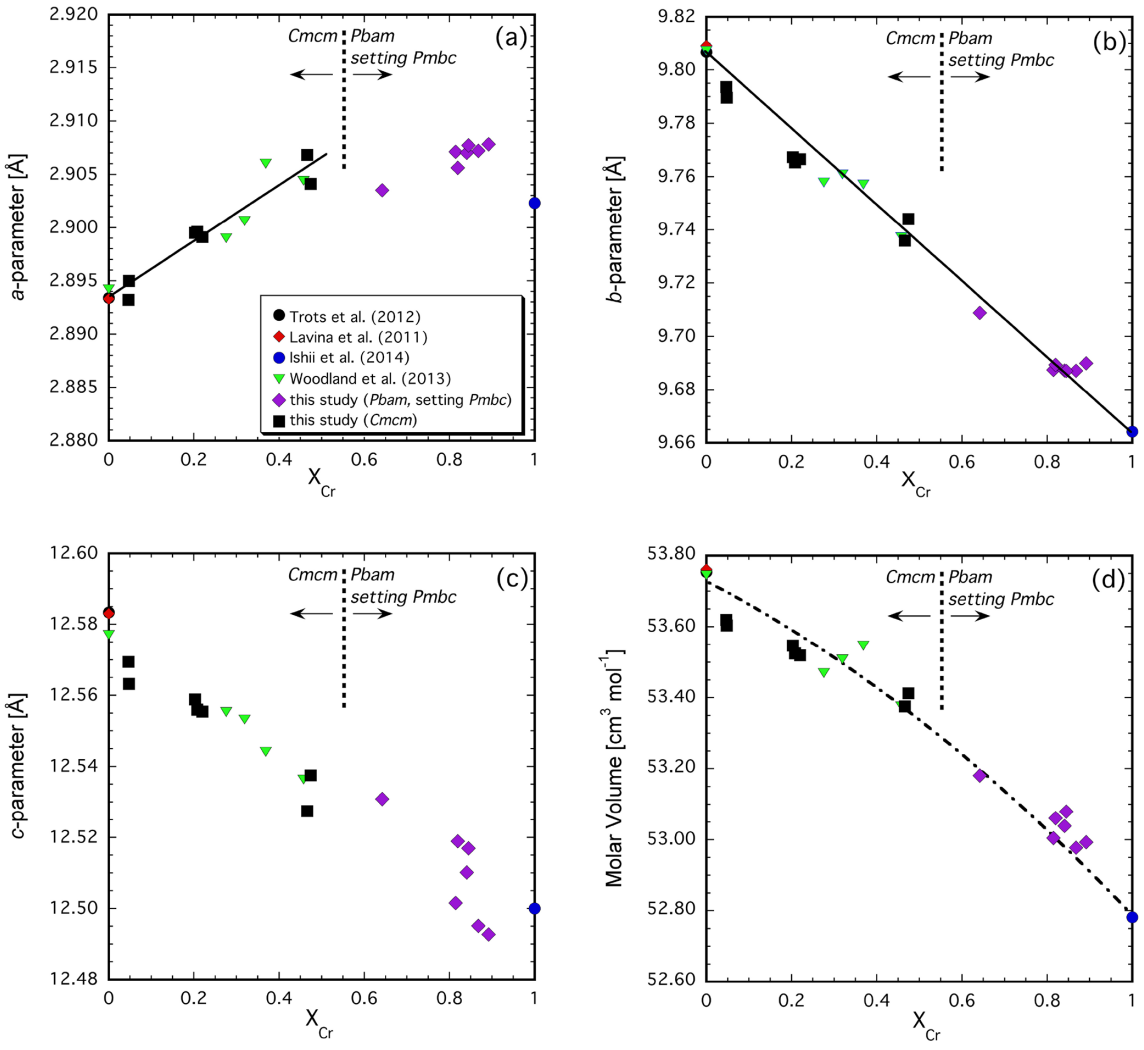

Figure 4. Variation in unit-cell parameters **(a)**, **(b)** and **(c)** and molar volume **(d)** across the Fe_4O_5–$Fe_2Cr_2O_5$ join. Note that the two endmembers have somewhat different structures so that the Cr-rich *Pbam* structure type has been transformed into the *Pmcb* space group in order to be directly comparable with the *Cmcm* structure type of the Fe^{3+}-bearing endmember (see text for details).

Fe^{3+}-free $Fe_2^{2+}Cr_2O_5$ endmember is smaller than our Fe^{3+}-bearing compositions (Fig. 4a).

In spite of the complexity exhibited by the unit-cell parameters and the change in crystal structure, the variation in molar volume with composition is rather well behaved across the join (Fig. 4d). Some scatter in the data may be attributable to somewhat different cation distributions (partially) quenched from differing experimental conditions as alluded to previously (Table 2). A weighted fit with a symmetric solution model yields a small interaction parameter of $W_v = 0.32(10)\,cm^3\,mol^{-1}$ ($n = 22$), along with endmember molar volumes of $53.73(1)\,cm^3\,mol^{-1}$ for Fe_4O_5 and $52.79(1)\,cm^3\,mol^{-1}$ for $Fe_2Cr_2O_5$. However, this model likely does not capture subtle structural changes since the nearly ideal behavior cannot be due to merely simple deflation of the structure as the smaller Cr cation progressively substitutes for Fe^{3+}. There must be a complex interplay between the different structural units as cation occupancies change and electron hopping between Fe^{2+} and Fe^{3+} becomes more difficult with Cr substitution, as discussed with regard to the unit-cell parameters.

The structure–composition systematics in Mg-bearing compositions can be assessed similarly but with the caveats that the dataset is smaller and that a small and variable amount of Fe^{2+} is additionally present due to minor reduction that occurred during the experiment (see above). The unit-cell parameters and molar volume that we obtain for the $Mg_2Cr_2O_5$ endmember are systematically smaller than those reported by Ishii et al. (2015) (Fig. 5a–d). In Fig. 5a, b and c, the unit-cell parameters of the solid solutions are plotted to account for the change in crystal structure across the join, as was done previously for the Fe^{2+} system (see above). Note

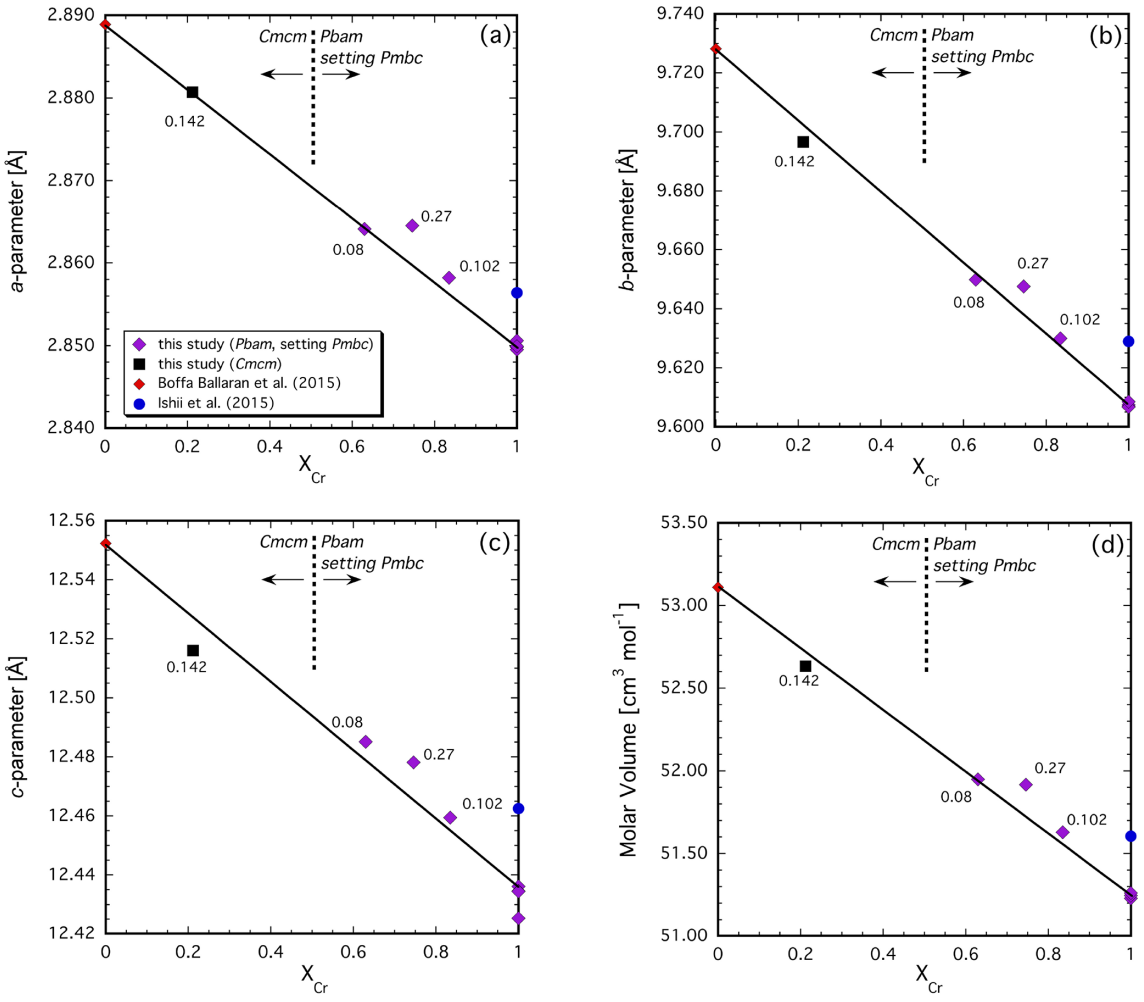

Figure 5. Variation in unit-cell parameters **(a)**, **(b)** and **(c)** and molar volume **(d)** across the $Mg_2Fe_2O_5$–$Mg_2Cr_2O_5$ join. Note that the two endmembers have somewhat different structures so that the Cr-rich *Pbam* structure type has been transformed into the *Pmcb* space group in order to be directly comparable with the *Cmcm* structure type (see text for details). Values given are the additional cations Fe^{2+} per formula unit that formed by reduction during the experiment.

that the short cell parameter systematically decreases with increasing Cr content (Fig. 5a). In spite of the structural transition, which must occur near the middle of the join (Table 3), the unit-cell parameters and molar volumes appear to behave close to linearly across the join. It is noteworthy that the sample with the smallest amount of additional Fe^{2+} (0.08 cations Fe^{2+} p.f.u. in Z2386u, Table 4) lies either on or very close to the tie line connecting the two endmember compositions (Fig. 5a–d). However, our one solid solution with the *Cmcm* structure type always plots below this tie line even though it contains an additional 0.142(5) c.p.f.u. Fe^{2+} (Fig. 5a–d). Considering that the ionic radius of Fe^{2+} is larger than that of Mg (Shannon, 1976), the unit-cell parameters of this sample would be expected to be somewhat larger than for Fe^{2+}-free compositions and not smaller. This is indeed the case for the other three samples in our dataset that have the *Pbam* structure (Fig. 5a–c). As with the $Fe_2(Cr,Fe^{3+})_2O_5$ solid solutions, complex structural effects related to changing cation distributions are clearly present. Unfortunately, our limited number of sample compositions does not currently permit a more thorough assessment of the Mg-bearing system, especially in the presence of additional Fe^{2+} whose site occupancy is currently unknown and is likely to be complex.

3.4 Associated oxide phases

3.4.1 Wüstite in the Fe^{2+}–Cr–Fe^{3+}–O system

Wüstite occurs together with the O_5 phase in virtually all experimental run products, which is consistent with mass balance (Table 1). Microprobe analysis indicates incorporation of up to 9 wt % Cr_2O_3 in wüstite (0.11 c.p.f.u. on a one-oxygen basis, Table 1). Logically, the starting bulk composition of a sample directly influences the Cr content of wüstite; temperature seems to have only a minor effect. Comparing

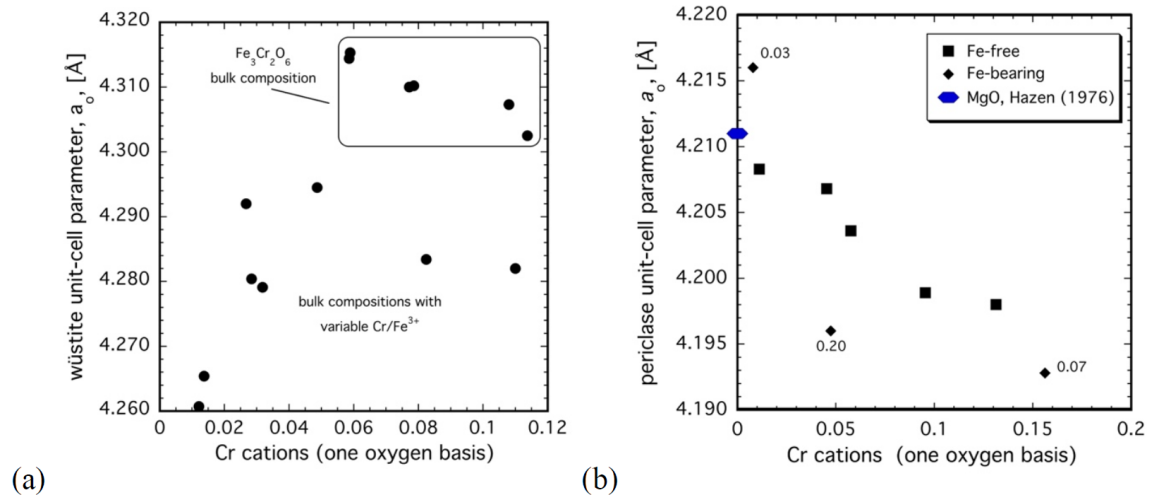

Figure 6. Variation in the unit-cell parameter as a function of composition of **(a)** Cr-bearing wüstite and **(b)** Cr-bearing periclase coexisting in the run products of our experiments. The values given for the two samples are the additional Fe contents in cations on a one-oxygen basis.

the six samples with the same $Fe_3Cr_2O_6$ bulk composition reveals that the incorporation of Cr leads to a small decrease in the unit-cell parameter (Fig. 6a, Table 1). Based on the composition of the coexisting O_5 phase, these samples are expected to contain a minimum of Fe^{3+}. On the other hand, wüstite in Fe^{3+}-rich bulk compositions tends to have low Cr contents but at the same time exhibit much smaller unit-cell parameters (Fig. 6a). This indicates that the substitution of Fe^{3+} into wüstite has a much larger effect on the molar volume than Cr^{3+} does, even though the substitution mechanism for these two trivalent cations should, in principle, be similar.

3.4.2 Periclase

Analysis of the run products of our Mg-bearing experiments reveals a significant Cr content in coexisting periclase. From EPMA, up to 25 wt % Cr_2O_3 (i.e., ∼ 0.16 c.p.f.u. Cr on a one-oxygen basis) can be incorporated into periclase at high temperatures (i.e., 1400 °C at 14 GPa), with less present at lower temperatures and higher pressures (Table 3). The unit-cell parameter of the coexisting periclase exhibits a distinct variation as a function of Cr content. Compared to pure MgO (Hazen, 1976), the addition of up to 0.13 c.p.f.u Cr in our Fe-free bulk compositions leads to a shortening of the unit-cell parameter by ∼ 0.013 Å, which equates to a lowering of the molar volume by ∼ 0.104 cm^3 mol^{-1} (Fig. 6b, Table 3).

3.4.3 High-*P* polymorphs of (Fe,Mg)Cr_2O_4

Run products from several experiments conducted at 18 and 20 GPa contained traces of high-*P* polymorphs with MCr_2O_4 stoichiometry (where M = Mg or Fe^{2+}), as detected in the powder XRD patterns (Tables 1, 3). The obtained unit-cell parameters and molar volume for $FeCr_2O_4$ with the mCF-type structure (Table 2) agree well with those reported by Ishii et al. (2014). In Mg-bearing compositions, our structural data for the $MgCr_2O_4$ endmember with the CT structure type (Table 4) are consistent with Ishii et al. (2015) but deviate somewhat from those given by Bindi et al. (2014). Analysis of the CT-structured phase in sample Z2281u indicates that substitution of nearly half of the Cr for Fe^{3+} leads to an increase in molar volume of ∼ 0.73 cm^3 or slightly less than 2 % (Table 4).

4 Implications

Although Fe_5O_6 has been demonstrated to be stable over a large range of pressure and temperature (Hikosaka et al., 2019; Woodland et al., 2023), its potential occurrence as an accessory phase in the Earth's deep mantle is limited due to its inability to form significant solid solution with other major and minor elements. For example, only minor amounts of Mg can be incorporated into the Fe_5O_6 structure (Woodland et al., 2023). In terms of trivalent cations, this current study indicates that Cr is for all practical purposes excluded from the Fe_5O_6 structure. Likewise, the experimental study by Schollenbruch et al. (2011) on the phase relations of hercynite ($FeAl_2O_4$) revealed a large P–T stability field for the assemblage wüstite + corundum, which would also seem to rule out significant solution of Al in Fe_5O_6. Thus, the potential mechanism for varying the Fe^{3+} / ∑Fe of Fe_5O_6 through trivalent cation substitution does not appear to be significant. However, the rare occurrence of nearly pure Fe oxides as inclusions in diamond (e.g., Stachel et al., 1998; Jacob et al., 2016) indicates there are certain Fe-rich environments in the deep mantle where Fe_5O_6 could occur and could even be associated with diamond formation.

The crystal chemical behavior of Fe_5O_6 contrasts with that of Fe_4O_5, where more extensive solid solution and other end-

member compositions with O_5 stoichiometry have been experimentally documented in this and other studies (see below). An explanation must lie with the structural difference between the two phases, namely that Fe_5O_6 contains double layers of edge-sharing FeO-like octahedra stacked between Ca-ferrite-structured layers instead of a single layer of octahedra as in Fe_4O_5 (compare Fig. 3c and b; Evrard et al., 1980). Along with additional octahedral sites, the Ca-ferrite layer in both phases also comprises a larger 6-fold coordinated site in the form of a bi-capped triangular prism (Fig. 3b, c; Evrard et al., 1980). The incorporation of Mg into Fe_5O_6 is limited to the ~ 27 mol % $Mg_3Fe_2O_6$ component, and inspection of the unit-cell parameters reported by Woodland et al. (2023) for this small compositional range reveals the same systematics as described above for Fe_4O_5–$Fe_2Cr_2O_5$ solid solutions: the direction of the intermediate length (*b* in the *Cmcm* structure type) decreases the most, and the shortest parameter (*a* in *Cmcm*) exhibits a small increase in length (compare data from Woodland et al., 2023, with data presented in Table 2). It is notable that the magnitudes of the change in unit-cell parameters of Mg-bearing Fe_5O_6 with up to just ~ 27 mol % $Mg_3Fe_2O_6$ are already half of those observed across the entire Fe_4O_5–$Fe_2Cr_2O_5$ join. Thus, it is perhaps unsurprising that the O_6 phase becomes destabilized at even relatively low Mg contents. As for Cr substituting for Fe^{3+} into the O_6 structure, the geometry of the double layers of octahedra is not as flexible as a single layer in accommodating a smaller cation with particular site preferences and yet remain compatible with the intervening prismatic sites occupied by Fe^{2+}. As it is, Cr incorporation into Fe_4O_5 leads to a phase transition halfway across the join in order to relieve lattice strain. The required puckering of the double octahedral layers of the O_6 phase may not be possible; hence, next to no Cr can be incorporated into Fe_5O_6, and no compositions along the $Mg_3Fe_2O_6$–$Mg_3Cr_2O_6$ join are stable.

The high-*P* post-spinel phase with O_5 stoichiometry exhibits a much greater ability to accommodate different divalent and trivalent cations. Complete solid solution in the $Fe^{2+}_2Fe^{3+}_2O_5$–$Mg_2Fe^{3+}_2O_5$ system was observed by Uenver-Thiele et al. (2018). Our current study indicates complete solid solution for the $Fe^{2+}_2Fe^{3+}_2O_5$–$Fe^{2+}_2Cr_2O_5$ and $Mg_2Fe^{3+}_2O_5$–$Mg_2Cr_2O_5$ binaries that likely extends to more complex $(Mg,Fe^{2+})_2(Fe^{3+},Cr)_2O_5$ compositions. As previously mentioned, a phase transition from the $CaFe_3O_5$ structure type (*Cmcm*) to the modified ludwigite structure type (*Pbam*) occurs to accommodate the increasing Cr substitution across the join. The formation of O_5-structured phases containing Al is more nuanced. Enomoto et al. (2009) synthesized the $Mg_2Al_2O_5$ endmember also with the modified ludwigite-type structure. On the other hand, the Fe analog $Fe_2Al_2O_5$ is not stable according to the work of Schollenbruch et al. (2010), and the incorporation of Al into Fe_4O_5 is limited to a maximum of 0.3 c.p.f.u (Uenver-Thiele et al., 2024). This restricts the possible range of O_5 solid solutions involving Al. However, in any case the dominant sink for Al in a pyrolitic mantle at high pressures will be garnet. It is the occurrence of Fe^{3+} that can be expected to stabilize Mg–Fe oxides as accessory phases, and the apparent structural flexibility of the O_5 phase makes it the most likely of the family of post-spinel phases to occur in a variety of environments at depths ranging from the deep upper mantle through the transition zone and into the upper parts of the lower mantle. At even higher pressures, a phase with O_4 stoichiometry becomes stable and may take on a variety of crystal structures (e.g., CT, CF and mCF types or others; Uenver-Thiele et al., 2017b; Ishii et al., 2014, 2015, 2020; Dubrovinsky et al., 2003) depending on the exact composition and particular P–T conditions.

The observation that both periclase and wüstite can incorporate non-negligible amounts of Cr at high pressures and temperatures suggests that Cr-bearing oxides could exsolve from ferropericlase during uplift from the transition zone or deeper. This is consistent with the minor Cr contents reported for some ferropericlase inclusions in diamond that are considered to have a deep origin, as well as the composition of fine-grained exsolved magnesioferrite grains found within some of the ferropericlase inclusions (e.g., Palot et al., 2016; Wirth et al., 2014; Stachel et al., 2000). Our study was not exhaustive in this regard, and a more systematic study of Cr incorporation into ferropericlase is warranted, as it may help provide constraints on the redox conditions attending diamond formation.

Data availability. All data obtained are presented in Tables 1, 2, 3 and 4 with supporting information provided in the figures.

Author contributions. ABW and LUT conceptualized the project in coordination with TBB. ABW secured the financial support. Experiments were conducted by ABW, LUT, KS, KR and CM. Sample analysis and data evaluation were carried out by ABW, LUT, KS, KR and TBB, with EB undertaking the synchrotron-based crystallographic investigation of sample Z2281u. All authors contributed to the preparation of the paper.

Competing interests. At least one of the (co-)authors is a member of the editorial board of *European Journal of Mineralogy*. The peer-review process was guided by an independent editor, and the authors also have no other competing interests to declare.

Disclaimer. Publisher's note: Copernicus Publications remains neutral with regard to jurisdictional claims made in the text, published maps, institutional affiliations, or any other geographical representation in this paper. While Copernicus Publications makes every effort to include appropriate place names, the final responsibility lies with the authors.

Special issue statement. This article is part of the special issue "Probing the Earth: experiments on and for our planet". It is a result of the EMPG 2023 conference, Milan, Italy, 12–15 June 2023.

Acknowledgements. This study was financially supported by the Deutsche Forschungsgemeinschaft (DFG) with funding awarded to Alan B. Woodland (Wo 652/35-1). Elena Bykova acknowledges the support of the DFG (Emmy Noether Programme, project no. BY 101/2–1). We thank Thomas Kautz and Tony Withers for their technical assistance with the multi-anvil presses in Frankfurt and Bayreuth. Nils Prawitz and Maria Blatt are acknowledged for their expert preparation of the microprobe mounts. Dominik Hezel and Natalia Sennova are thanked for their help in obtaining the microprobe analyses and powder diffraction patterns, respectively.

Financial support. This research has been supported by the Deutsche Forschungsgemeinschaft (grant no. Wo 652/35-1 and project no. BY 101/2–1).

This open-access publication was funded
by Goethe University Frankfurt.

Review statement. This paper was edited by Francois Holtz and reviewed by two anonymous referees.

References

Armstron, J. T.: CITZAFF: A package of correction programs for the quantitative electron microbeam X-ray analysis of thick polished materials, thin films, and particles, Microbeam Anal., 4, 177–200, 1995.

Aslandukov, A., Aslandukov, M., Dubrovinskaia, N., and Dubrovinsky, L.: Domain Auto Finder (DAFi) program: the analysis of single-crystal X-ray diffraction data from polycrystalline samples, J. Appl. Crystal., 55, 1383–1391, 2022.

Bindi, L., Sirotkina, E., Bobrov, A. V., and Irifune, T.: X-ray single-crystal structural charaterization of $MgCr_2O_4$, a post-spinel phase synthesised at 23 GPa and 1600 °C, J. Phys. Chem. Solid., 75, 638–641, 2014.

Bindi, L., Sirotkina, E., Bobrov, A. V., and Irifune, T.: Structural and chemical characterization of $Mg[(Cr,Mg)(Si,Mg)]O_4$, a new post-spinel phase with sixfold-corrdinated silicaon, Am. Mineral., 100, 1633–1636, 2015.

Boffa Ballaran, T., Uenver-Thiele, L., Woodland, A. B., and Frost, D. J.: Complete substitution of Fe^{2+} by Mg in Fe_4O_5: The crystal structure of the $Mg_2Fe_2O_5$ end-member, Am. Mineral., 100, 628–632, 2015.

Brey, G. P., Bulatov, V., and Girnis, A.: Geobarometry for peridotites: experiments in simple and natural systems from 6 to 10 GPa, J. Petrol., 49, 3–24, 2008.

Chen, M., Shu, J., Xie, X., and Mao, H.-K.: Natural $CaTi_2O_4$-structure $FeCr_2O_4$ polymorph in Suizhou meteorite and its significance in mantle mineralogy, Geochim. Cosmochim. Ac., 67, 3937–3942, 2003a.

Chen, M., Shu, J., Mao, H.-K., Xie, X., and Hemley, R. J.: Natural occurrence and synthesis of two new postspinel polymorphs of chromite, P. Natl. Acad. Sci. USA, 100, 14651–14654, 2003b.

CrysAlisPro Software system, version 1.171.40.84a, Rigaku Oxford Diffraction, Oxford, UK, 2019.

Decker, B. F. and Kasper, J. S.: The structure of calcium ferrite, Acta Cryst., 10, 332–337, https://doi.org/10.1107/S0365110X5700095X, 1957.

Dieckmann, R.: Defects and Cation Diffusion in Magnetite (IV): Nonstoichiometry and Point Defect Structure of Magnetite ($Fe_{3-\delta}O_4$). Bericht der Bunsenges, J. Phys. Chem.-US, 86, 112–118, 1982.

Dubrovinsky, L. S., Dubrovinskaia, N. A., McCammon, C., Rozenberg, G. Kh., Ahuja, R., Osorio-Guillen, J. M., Dmitriev, V., Weber, H.-P., Le Bihan, T., and Johansson, B.: The structure of the metallic high-pressure Fe_3O_4 polymorph: experimental and theoretical study, J. Phys. Cond. Mat., 15, 7697–7706, 2003.

Enomoto, A., Kojitani, H., Akaogi, M., Miura, H., and Yusa, H.: High-pressure transitions in $MgAl_2O_4$ and a new high-pressure phase of $Mg_2Al_2O_5$, J. Solid State Chem., 182, 389–395, 2009.

Evrard, O., Malaman, B., Jeannot, F., Courtois, A., Alebouyeh, H., and Gerardin, R.: Mise en évidence de $CaFe_4O_6$ et détermination des structures cristallines des ferrites de calcium $CaFe_{2+n}O_{4+n}$ ($n = 1, 2, 3$): nouvel exemple d'intercroissance, J. Solid State Chem., 35, 112–119, 1980.

Fei, Y. W., Frost, D. J., Mao, H. K., Prewitt, C. T., and Häusermann, D.: In situ structure determination of the high-pressure phase of Fe_3O_4, Am. Mineral., 84, 203–206, 1999.

Hazen, R. M.: Effects of temperature and pressure on the cell dimension and X-ray temperature factors of periclase, Am. Mineral., 61, 266–271, 1976.

Hikosaka, K., Sinmyo, R., Hirose, K., Ishii, T., and Ohishi, Y.: The stability of Fe_5O_6 and Fe_4O_5 at high pressure and temperature, Am. Mineral., 104, 1356–1359, 2019.

Inoue, T., Irfune, T., Higo, Y., Sanehira, T., Sueda, Y., Yamada, A., Shinmei, T., Yamazaki, D., Ando, J., Funakoshi, K., and Utsumi, W.: The phase boundary between wadsleyite and ringwoodite in Mg_2SiO_4 determined by in situ Xray diffraction, Phys. Chem. Miner., 33, 106–114, 2006.

Ishii, T., Kojitani, H., Tsukamoto, S., Fujino, K., Mori, D., Inaguma, Y., Tsujino, N., Yoshino, T., Yamazaki, D., Higo, Y., Funakoshi, K., and Akaogi, M.: High-pressure phase transitions in $FeCr_2O_4$ and structure analysis of new post-spinel $FeCr_2O_4$ and $Fe_2Cr_2O_5$ phases with meteoritical and petrological implications, Am. Mineral., 99, 1788–1797, 2014.

Ishii, T., Kojitani, H., Fujino, K., Yusa, H., Mori, D., Inaguma, Y., Matsushita, Y., Yamaura, K., and Akaogi, M.: High-pressure high-temperature transitions in $MgCr_2O_4$ and crystal structures of new $Mg_2Cr_2O_5$ and post-spinel $MgCr_2O_4$ phases with implications for ultrahigh-pressure chromitites in ophiolites, Am. Mineral., 100, 59–65, 2015.

Ishii, T., Uenver-Thiele, L., Woodland, A., Alig, E., and Boffa Ballaran, T.: Synthesis and crystal structure of Mg-bearing Fe_9O_{11}: New insight in the complexity of Fe-Mg oxides at conditions of the deep upper mantle, Am. Mineral., 103, 1873–1876, 2018.

Ishii, T., Miyajima, N., Sinmyo, R., Kojitani, H., Mori, D., Inaguma, Y., and Akaogi, M.: Discovery of new-structured post-spinel $MgFe_2O_4$: Crystal structure and high-pressure

phase relations, Geophys. Res. Lett., 47, e2020GL087490, https://doi.org/10.1029/2020GL087490, 2020.

Jacob, D. E., Piazolo, S., Schreiber, A., and Trimby, P.: Redox-freezing and nucleation of diamond via magnetite formation in the Earth's mantle, Nat. Commun., 7, 11891, https://doi.org/10.1038/ncomms11891, 2016.

Keppler, H. and Frost, D. J.: Introduction to minerals under extreme conditions, in: Mineral Behaviour at Extreme Conditions, EMU Notes in Mineralogy, Heidelberg, Germany, 7, 1–30, https://doi.org/101180/EMU-notes.7, 2005.

Larson, A. C. and Von Dreele, R. B.: General structure analysis system (GSAS), Los Alamos National Laboratory Report, LAUR, 86–748, 2000.

Lavina, B., Dera, P., Kim, E., Meng, Y., Downs, R. T., Weck, P. F., Sutton, S. R., and Zhao, Y.: Discovery of the recoverable high-pressure iron oxide Fe_4O_5, P. Natl. Acad. Sci. USA, 108, 17281–17285, 2011.

Lavina, B. and Meng, Y.: Unraveling the complexity of iron oxides at high pressure and temperature: Synthesis of Fe_5O_6, Sci. Adv., 1, e1400260, https://doi.org/10.1126/sciadv.1400260, 2015.

Lenaz, D., Skogby, H., Princivalle, F., and Hålenius, U.: Structural changes and valence states in the $MgCr_2O_4$–$FeCr_2O_4$ solid solution series, Phys. Chem. Miner., 31, 633–642, https://doi.org/10.1007/s00269-004-0420-0, 2004.

Matrasova, E. A., Bobrov, A. V., Bindi, L., and Irifune, T.: Phase relations in the model system SiO_2–MgO–Cr_2O_3: Evidence from results of experiments in petrologicaly significant sections at 12–24 GPa and 1600 °C, Petrology, 26, 588–598, 2018.

Myhill, B., Ojwang, D. O., Ziberna, L., Frost, D., Boffa Ballaran, T., and Miyajima, N.: On the P-T-fO_2 stability of Fe_4O_5 and Fe_5O_6-rich phases: a thermodynamic and experimental study, Contrib. Mineral. Petr., 171, 1–11, 2016.

Nimis, P., Angel, R.J., Alvaro, M., Nestola, F., Harris, J. W., Casati, N., and Marone, F.: Crystallographic orientations of magnesiochromite inclusions in diamonds: what do they tell us?, Contrib. Mineral. Petr., 174, 29, https://doi.org/10.1007/s00410-019-1559-5, 2019.

O'Neill, H. S. T. C., and Dollase, W. A.: Crystal structures and cation distributions in simple spinels from powder XRD structural refinements: $MgCr_2O_4$, $ZnCr_2O_4$, Fe_3O_4 and the temperature dependence of the cation distribution in $ZnCr_2O_4$, Phys. Chem. Miner., 20, 541–555, 1994.

Palot, M., Jacobsen, S. D., Townsend, J. P., Nestola, F., Marquardt, K., Miyajima, N., Harris, J. W., Stachel, T., McCammon, C. A., and Pearson, D. G.: Evidence for H_2O-bearing fluids in the lower mantle from diamond inclusion, Lithos, 265, 237–243, 2016.

Schollenbruch, K., Woodland, A. B., and Frost, D. J.: The stability of hercynite at high pressures and temperatures, Phys. Chem. Miner., 37, 137–143, https://doi.org/10.1007/s00269-009-0317-z, 2010.

Schollenbruch, K., Woodland, A. B., Frost, D. J., Wang, Y., Sanehira, T., and Langenhorst, F.: In situ determination of the spinel – post-spinel transition in Fe_3O_4 at high temperature and pressure by synchrotron X-ray diffraction, Am. Mineral., 96, 820–827, https://doi.org/10.2138/am.2011.3642, 2011.

Shannon, R. D.: Revised effective ionic radii and systematic studies of interatomic distances in halides and chalcogenides, Acta Cryst., A32, 751–767, 1976.

Sinmyo, R., Bykova, E., Ovsyannikov, S. V., McCammon, C., Kupenko, I., Ismailova, L., and Dubrovinsky, L.: Discovery of Fe_7O_9: a new iron oxide with a complex monoclinic structure, Sci. Rep., 6, 32852, https://doi.org/10.1038/srep32852, 2016.

Sirotkina, E. A., Bobrov, A. V., Bindi, L., and Irifune, T.: Chromium-bearing phases in the Earth's mantle: Evidence from experiments in the Mg_2SiO_4–$MgCr_2O_4$ system at 10–24 GPa and 1600 °C, Am. Mineral., 103, 151–160, 2018.

Stachel, T. and Harris, J. W.: The origin of cratonic diamonds – Constraints from mineral inclusions, Ore Geol. Rev., 34, 5–32, 2008.

Stachel, T., Harris, J. W., and Brey, G. P.: Rare and unusual mineral inclusions in diamonds from Mwadui, Tanzania, Contrib. Mineral. Petr., 132, 34–47, 1998.

Stachel, T., Harris, J. W., Brey, G. P., and Joswig, W.: Kankan diamonds (Guinea): II. Lower mantle inclusion paragenesis, Contrib. Mineral. Petr., 140, 34–47, 2000.

Stachel, T., Harris, J. W., Tappert, R., and Brey, G. P.: Peridotitic diamonds from the Slave and Kaapvaal cratons – similarities and differences based on a preliminary data set, Lithos, 71, 489–503, 2003.

Toby, B. H.: EXPGUI, a graphical user interface for GSAS. J. Appl. Crystallogr., 34, 210–213, 2001.

Trots, D. M., Kurnosov, A., Woodland, A. B., and Frost, D. J.: The thermal breakdown of Fe_4O_5 at ambient pressure, European Mineralogical Conference, 2–6 September 2012, Frankfurt, Germany, EMC2012-556-1, 2012.

Uenver-Thiele, L., Woodland, A. B., Boffa Ballaran, T., Miyajima, N., and Frost, D. J.: Phase relations of $MgFe_2O_4$ at conditions of the deep upper mantle and transition zone, Am. Mineral., 102, 632–642, 2017a.

Uenver-Thiele, L., Woodland, A. B., Boffa Ballaran, T., Miyajima, N., and Frost, D. J.: Phase relations of Fe-Mg spinels including new high-pressure post-spinel phases and implications for natural samples, Am. Mineral., 102, 2054–2064, 2017b.

Uenver-Thiele, L., Woodland, A. B., Miyajima, N., Boffa Ballaran, T., and Frost, D. J.: Behavior of Fe_4O_5−$Mg_2Fe_2O_5$ solid solutions and their relation to coexisting Mg-Fe silicates and oxide phases, Contrib. Mineral. Petr., 173, 20, https://doi.org/10.1007/s00410-018-1443-8, 2018.

Uenver-Thiele, L., Woodland, A. B., Miyajima, N., Boffa Ballaran, T., Alig, E., and Fink, L.: High-P-T phase relations of Al-bearing magnetite: Post-spinel phases as indicators for P-T conditions of formation of natural samples, Am. Mineral., 109, 1062–1073, https://doi.org/10.2138/am-2023-8948, 2024.

Wirth, R., Dobrzhinetskaya, L., Harte, B., Schreiber, A., and Green, H. W.: High-Fe (Mg, Fe)O inclusion in diamond apparently from the lowermost mantle, Earth. Planet. Sc. Lett., 404, 365–375, 2014.

Woodland, A. B., Frost, D. J., Trots, D. M., Klimm, K., and Mezouar, M.: In situ observation of the breakdown of magnetite (Fe_3O_4) to Fe_4O_5 and hematite at high pressures and temperatures, Am. Mineral., 97, 1808–1811, 2012.

Woodland, A. B., Schollenbruch, K., Koch, M., Boffa Ballaran, T., Angel, R. J., and Frost, D. J.: Fe_4O_5 and its solid solutions in several simple systems, Contrib. Mineral. Petrol., 166, 1677–1686, 2013.

Woodland, A. B., Uenver-Thiele, L., and Boffa Ballaran, T.: Synthesis of Fe_5O_6 and the High-Pressure Stability of Fe^{2+}-Fe^{3+}-oxides related to Fe_4O_5, Goldschmidt Abs, 2015, 3446, 2015.

Woodland, A. B., Uenver-Thiele, L., Boffa Ballaran, T., Miyajima, N., Rosbach, K., and Ishii, T.: Stability of Fe_5O_6 and its relation to other Fe-Mg oxides at high pressures and temperatures, Am. Mineral., 108, 140–149, 2023.